Electronic Supplementary Information

Rational design of dual-gradient zincophilic-conductive interphase for dendrite-free zinc batteries

Xunwen Zheng,[a] Ziyang Song,[a] Da Zhang,[a] Wenyan Du,[a] Ling Miao,[a] Yaokang Lv,[b] Li Xie,[c, d] Lihua Gan,[a] Mingxian Liu,[a*]

[a] *Shanghai Key Lab of Chemical Assessment and Sustainability, School of Chemical Science and Engineering, Tongji University, Shanghai 200092, P. R. China*

[b] *College of Chemical Engineering, Zhejiang University of Technology, Hangzhou 310014, P. R. China*

[c] *Key Laboratory of Yangtze River Water Environment Ministry of Education, College of Environmental Science and Engineering, Tongji University, Shanghai 200092, P. R. China*

[d] *Shanghai Institute of Pollution Control and Ecological Security, Shanghai 200092, P. R. China*

Section S1. Supplementary methods

1.1 Characterizations

X-ray diffraction (XRD) patterns were obtained on D8 Advance X-ray diffractometer (Cu Kα radiation). Fourier-transformed infrared spectrum (FT-IR) was monitored using Thermo Nicolet NEXUS spectrometer. Morphological and elemental images were acquired using scanning electron microscopy (SEM, Hitachi S-4800) equipped with X-ray energy dispersive spectroscopy (EDS) instrument. Transmission electron microscopy (TEM, JEM-2100) was applied to observe sample nanostructures. Nitrogen sorption isotherm was analyzed on Micromeritics ASAP 2460 apparatus at −196 °C. The surface area was obtained by the Braunauer-Emmett-Teller method. The pore size distribution was evaluated by the nonlocal density functional theory model. The surface chemistry was studied by an X-ray photoelectron spectrometer (XPS, AXIS Ultra DLD). Nanoscale surface potential measurement was taken with a scanning probe microscope (SPM-9700HT). Thermal stability was tested on a STA409 PC thermogravimetric (TG) analyzer in nitrogen atmosphere at a heating speed of 10 °C min^{-1}. Electronic conductivity was tested with a standard four-probe analyzer (ST2722-SD).

1.2 Electrochemical measurements

2032 coin-type cells were assembled for electrochemical tests in air atmosphere by using a glass fiber filter as the separator, and 2.0 M $ZnSO_4$ aqueous solution as the electrolyte. Symmetrical cells were fabricated by using two identical bare Zn or Zn electrodes equipped with different coatings. Asymmetric cells were assembled by using Cu foil or Cu electrodes equipped with different coatings as the working electrode, and Zn foil as the counter electrode. For the full battery tests, KVOH was employed as cathodes and bare Zn or CF/Ag-CF@Zn as anodes. The KVOH cathodes were prepared by mixing KVOH (70 wt%), graphite (20 wt%), and PVDF (10 wt%) in NMP solvent under vigorous stirring. The obtained slurry was cast onto a Ti disk with a KVOH loading mass of about 3−5 mg cm^{-2}. The cyclic voltammetry (CV), chronoamperometry (CA), linear sweep voltammetry (LSV), Tafel and electrochemical impedance spectroscopy (EIS) measurements were performed on a CHI660E electrochemical workstation. Galvanostatic charge/discharge (GCD)

measurements were conducted on the CT3001A battery test system.

1.3 Structure simulation of quasi-COF polymer structure

The initial structure model was built using the Forcite module in the Materials Studio software. Considering the propeller-like conformation of the central building blocks, we applied the space group with P1 symmetry. The model was then optimized using the Geometry Optimization and Energy routine, which includes energy minimization and cell parameter optimization. Based on this optimized model, we determined the unit cell parameters via Pawley refinement of the experimental XRD data until the R_P and R_{WP} values converge.

1.4 Calculation of relative texture coefficient

Relative texture coefficient (RTC) of Zn lattice plane was calculated by using the following formula:[1]

$$\mathrm{RCT}_{(hkl)} = \frac{I_{(hlk)}/I_{0(hlk)}}{\sum(I_{(hlk)}/I_{0(hlk)})} \times 100 \quad \text{(Eq. S1)}$$

where $I_{(hkl)}$ is the intensity obtained from the textured sample, and $I_{0(hkl)}$ is the intensity of the standard oriented sample.

1.5 Calculation of activation energy

Activation energy can be studied by the Arrhenius equation:[2]

$$R_{ct}^{-1} = A\exp(-E_a/RT) \quad \text{(Eq. S2)}$$

where R_{ct} is the charge-transfer resistance, A is the frequency factor, R is the gas constant, and T is the absolute temperature.

1.6 Calculation of Zn2+ transference number

Zn^{2+} transference number ($T_{Zn^{2+}}$) was evaluated in symmetrical Zn cells combined by EIS before and after the CA test, and calculated by the following equation:[3]

$$T_{Zn^{2+}} = \frac{(\nabla V / I_0 - R_0)}{(\nabla V / I_{ss} - R_{ss})} \quad \text{(Eq. S3)}$$

where (∇V = 20 mV) is the applied constant potential, I_{ss} and R_{ss} are the steady state current and

charge transfer resistance, respectively. I_0 and R_0 are the initial current and charge transfer resistance, respectively.

1.7 Calculation of ionic conductivity

The ionic conductivity (σ) can be calculated from Rs from EIS measurement according to the following equation:[4]

$$\sigma = \frac{L}{R_s S} \quad \text{(Eq. S4)}$$

where σ is the ionic conductivity, L is the Zn^{2+} diffusion distance. R_s and S are the electrolyte resistance and electrode surface, respectively

1.8 Calculation of exchange current density

Exchange current density is generally employed to evaluate the kinetics of Zn deposition, by the following equation:[5]

$$i = i_0 \frac{F}{RT} \cdot \frac{\eta}{2} \quad \text{(Eq. S5)}$$

where T, R, and F are the absolute temperature, the gas constant, and the Faraday's constant. i_0 is the operating current density, and η is the total overpotential.

1.9 Calculation of the depth of discharge (DOD) of Zn anode

The depth of discharge (DOD) of Zn anode was calculated using the following equation:[6]

$$\mathrm{DOD} = \frac{It}{mM} \cdot 100\% \quad \text{(Eq. S6)}$$

where I (mA) is the applied current density, t (h) is the discharge time, m (g) is the mass of the Zn in Zn anode, M (mAh g^{-1}) is the theoretical specific capacity of Zn (820 mAh g^{-1}).

1.10 Calculation of Zn^{2+} diffusion coefficient

Zn^{2+} diffusion coefficient ($D_{Zn^{2+}}$) was calculated by galvanostatic intermittent titration technique (GITT):[7]

$$D_{Zn^{2+}} = \frac{4L^2}{\pi t}\left(\frac{\Delta E_s}{\Delta E_t}\right)^2 \quad \text{(Eq. S7)}$$

Where t is the duration of the current pulse, ΔE_s is the steady-state potential change by the current pulse. ΔE_t is the potential change of the constant current pulse excluded the iR drop. L is ion diffusion length; for a compact electrode, it is equal to the thickness of the electrode. The galvanostatic intermittent titration technique (GITT) test was carried out at a constant current of 50 mA g^{-1} for an interval of 10 min and then suspended for 10 min at an open-circuit state.

1.11 Distribution of relaxation time analysis

Distribution of relaxation time (DRT) analysis was conducted *via* DRTtools (https://github.com/ciuccislab/DRTtools) supported by Francesco Ciucci. The hierarchical Bayesian approach was selected to analyze original EIS data coupled with the Gaussian method of discretization.[8-11]

1.12 Computational details

Density functional calculations were performed using the DMol^3 package in the Materials Studio software. The exchange-correlation interaction was described by Perdew-Burke-Ernzerhof functional with a generalized gradient approximation. A double numerical basis set with polarization functions was applied. The energy cutoff was set to 520 eV, and a gamma-centered 3 × 3 × 1 mesh was used for the k-points. A 15 Å vacuum space along the z direction was used. All atoms were allowed to relax during Zn adsorption. The binding energy (E_b) was calculated according to the following equations:

$$E_b = E_{total} - E_{sub} - E_{atom} \quad \text{(Eq. S8)}$$

E_{total}, E_{sub}, and E_{atom} represent the total energies of all systems, substrates, and Zn atoms, respectively.

Ion concentration fields were simulated based on COMSOL Multiphysics software. The models of electrochemical systems were constructed by the tertiary Nernest-Plank physical field associated with Fick's diffusion low, Butler-Volmer equation and Nernst-Einstein relation.

Section S2. Supporting characterizations

Fig. S1. Schematic diagram for the dual-gradient CF/Ag-CF@Zn electrode.

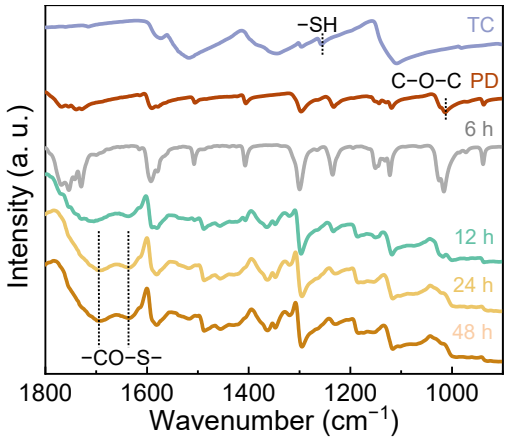

Fig. S2. FT-IR spectra of polymers at different polymerization times.

Notes to Fig. S2: During the transesterification reaction of TC and PD, the absorption bands of −SH (1255 cm^{-1}) and C−O−C (1014 cm^{-1}) gradually weaken, while typical absorption bands of −CO−S− (1690 and 1633 cm^{-1}) appear, providing the successful coupling of TC and PD.[12-14] Subsequently, the polymerization reaction stabilizes at 24 hours (h), and extending the reaction time does not lead to significant changes.

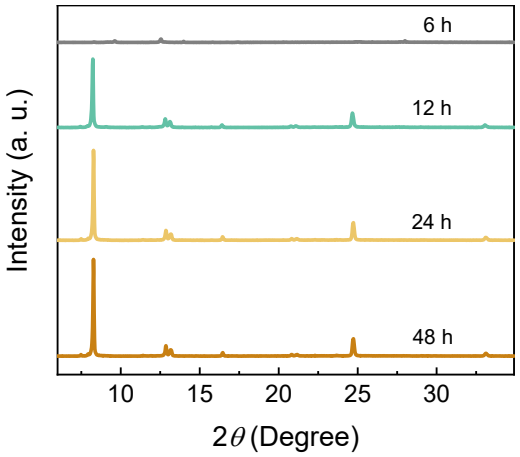

Fig. S3. XRD patterns of polymers at different polymerization times.

Notes to Fig. S3: The crystallinity regularity of the self-assembled polymer was evaluated using XRD patterns. As the polymerization proceeds, the crystallinity of the polymer increases and eventually stabilizes at 24 h.

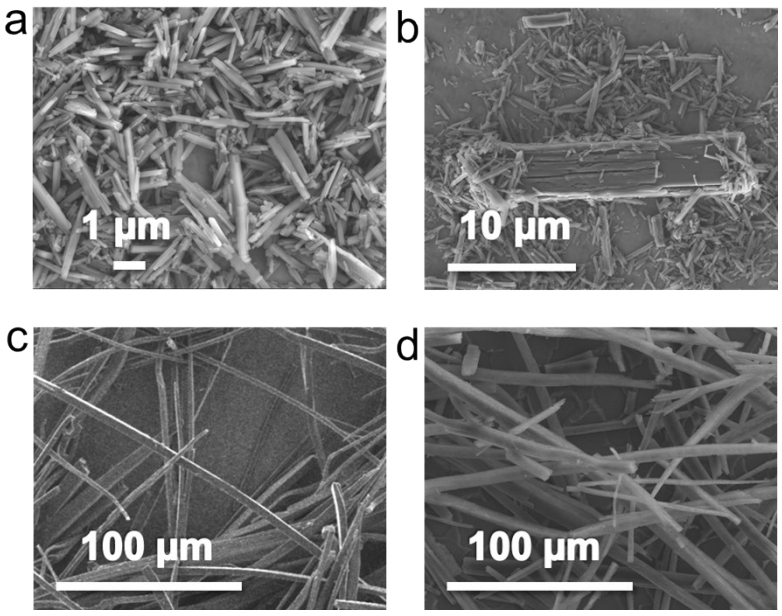

Fig. S4. Morphological evolution of polymers at different polymerization times of (a) 6 h, (b) 12 h, (c) 24 h, and (d) 48 h, respectively.

Notes to Fig. S4: SEM was employed to supervise the morphological transition from detrital particles to the higher-order fiber during the polymerization process. Based on the FT-IR, XRD, and SEM analyses of the polymer at different polymerization times, we find that polymerization stabilizes at 24 h. Extending the reaction time does not lead to significant changes. Meanwhile, the

spatiotemporally controlled self-assembly mechanism is revealed, in which the anhydride groups of PD could be unlocked and subsequently coupled with −SH groups of TC to yield detrital polymer nanoparticles bridged by thioester groups (elementary structure). This reaction is expected to facilitate the π–π interactions of the perylene-based building blocks and direct the self-assembly process of thioester-linked nanoparticles into quadrangular superstructures with clastic edges (secondary structure).[15] Lastly, these podgy quadrangular superstructures can extend into higher-order microscale fiber with a quadrangular section via electrostatic force (tertiary structure).[16]

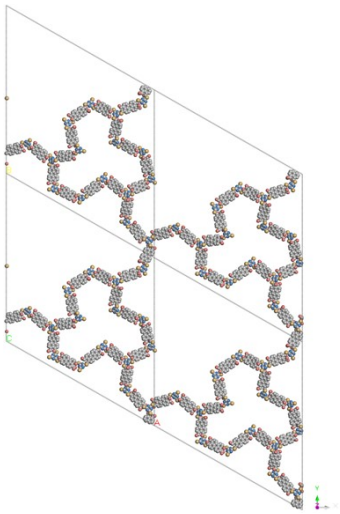

Fig. S5. The structural model of quasi-COF polymer with the eclipsed AA stacking model.

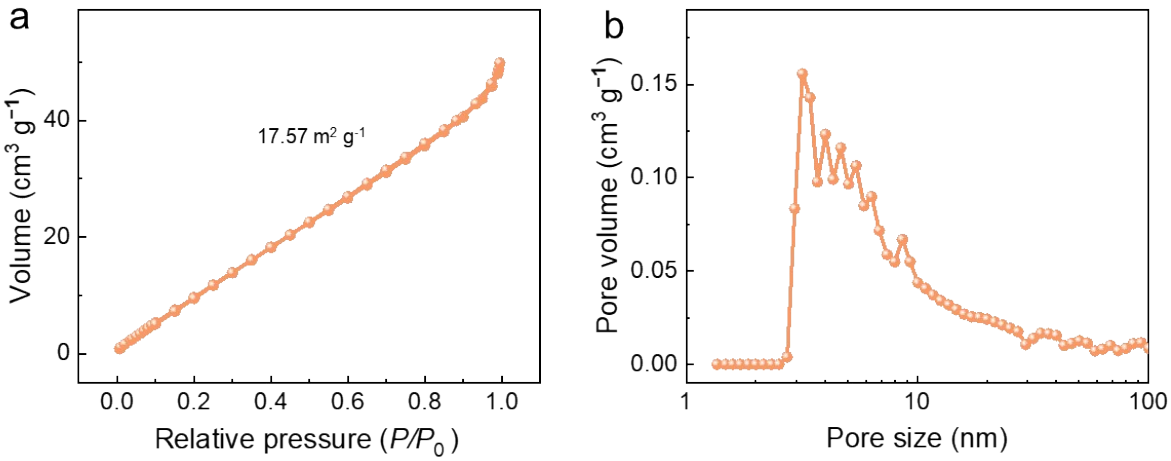

Fig. S6. (a) Nitrogen sorption isotherm and (b) corresponding pore size distribution curve of quasi-COF polymer.

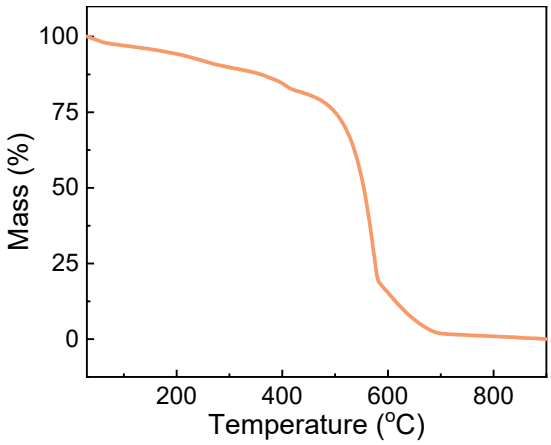

Fig. S7. Thermogravimetric analysis of quasi-COF polymer with a 24 h stable polymerization.

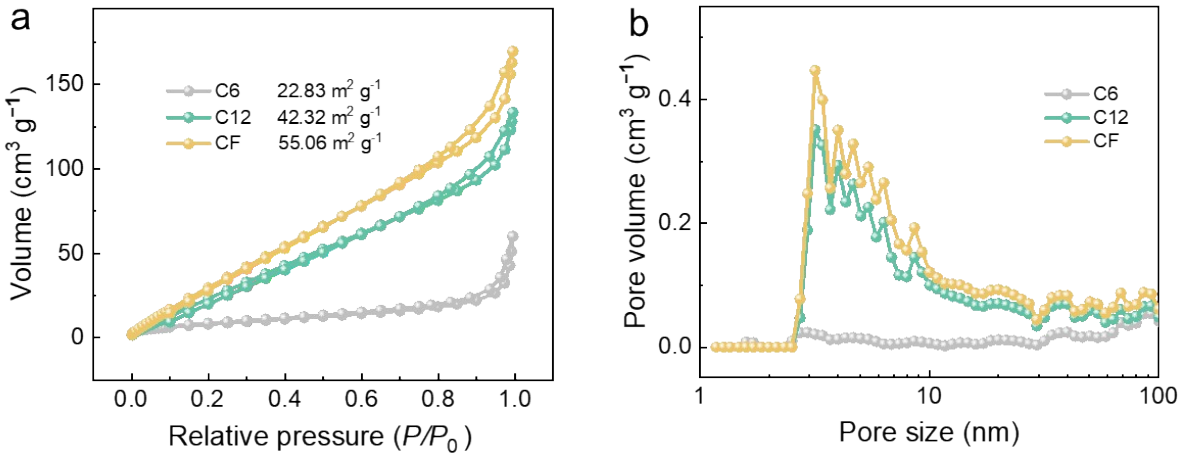

Fig. S8. (a) Nitrogen sorption isotherms and (b) corresponding pore size distribution curves of polymer-derived carbons with various polymerization times.

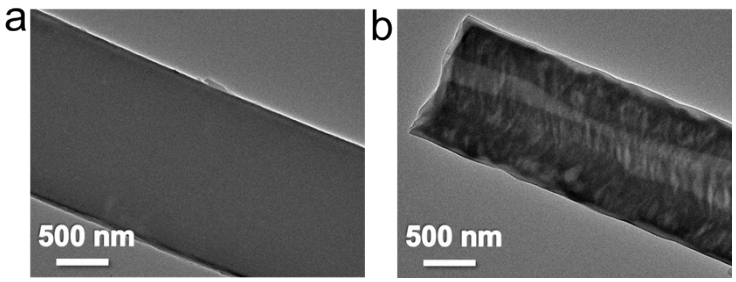

Fig. S9. TEM images of (a) quasi-COF polymer and (b) CF.

Table S1. Surface areas (S_{BET}), total pore volumes (V_{tol}) of polymer-derived carbons with various polymerization times.

Sample	C6	C12	CF
S_{BET} (m^2 g^{-1})	22.83	42.32	55.06
V_{tol} (cm^3 g^{-1})	0.08	0.20	0.25

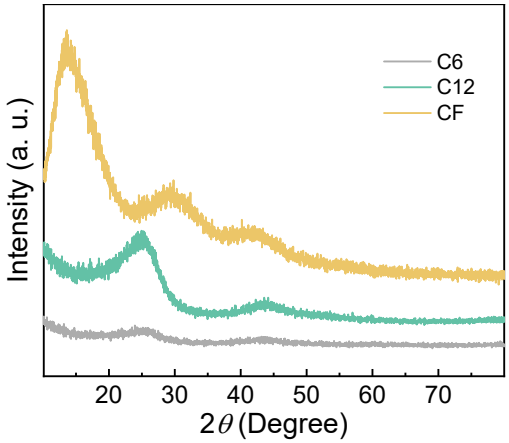

Fig. S10. XRD patterns of polymer-derived carbons with various polymerization times.

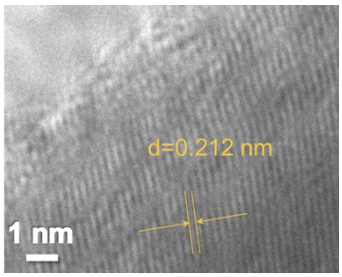

Fig. S11. High-resolution TEM image of Ag-CF.

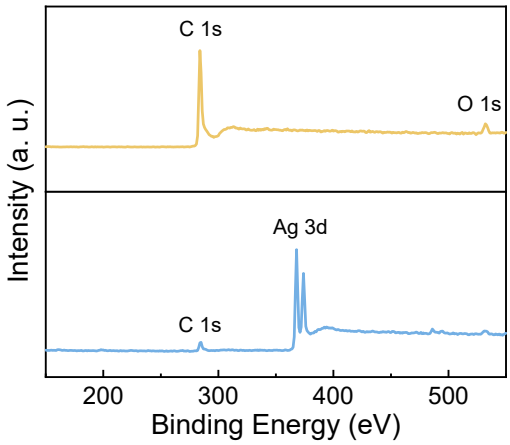

Fig. S12. Wide-scan XPS spectra of CF and Ag-CF.

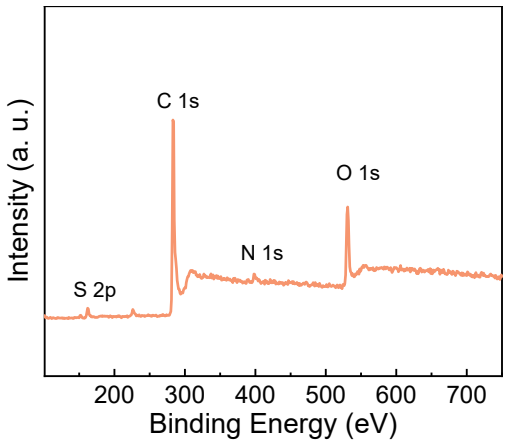

Fig. S13. Wide-scan XPS spectra of quasi-COF polymer.

Table S2. Chemical compositions of CF and Ag-CF.

Sample	C (wt.%)	O (wt.%)	Ag (wt.%)
CF	94.07	5.93	—
Ag-CF	15.19	4.44	80.37

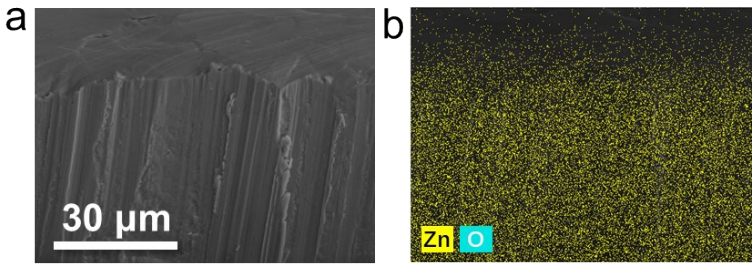

Fig. S14. Cross-sectional (a) SEM image and (b) EDS map of initial bare Zn.

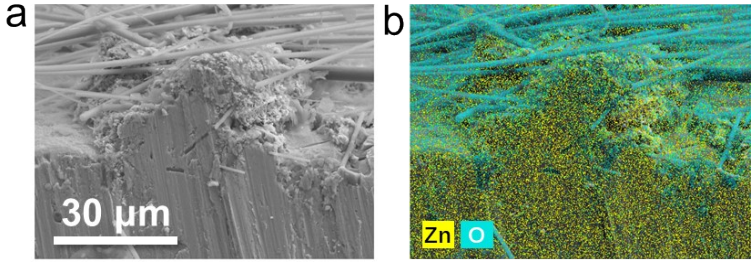

Fig. S15. Cross-sectional (a) SEM image and (b) EDS map of Zn after 30 cycles.

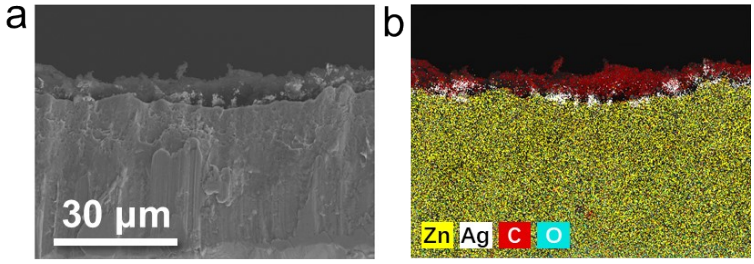

Fig. S16. Cross-sectional (a) SEM image and (b) EDS map of initial CF/Ag-CF@Zn.

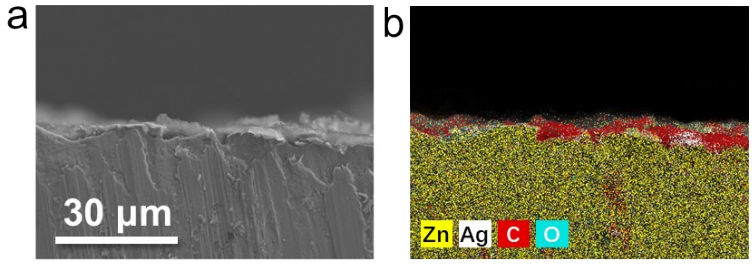

Fig. S17. Cross-sectional (a) SEM image and (b) EDS map of CF/Ag-CF@Zn after 30 cycles.

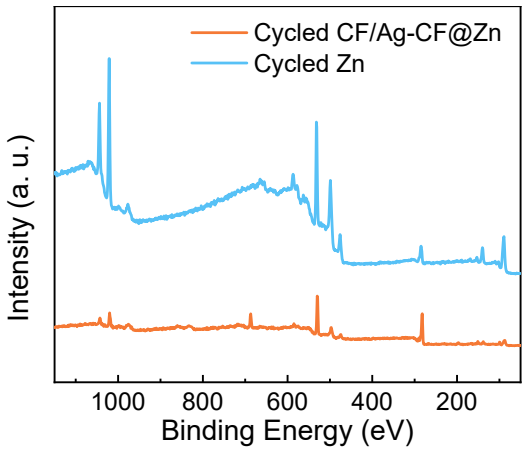

Fig. S18. Wide-scan XPS spectra of CF/Ag-CF@Zn and Zn after 30 cycles.

Notes to Fig. S18: The cycled Zn exposes more Zn signal (50.37 wt%) due to its direct contact with the electrolyte via the "top-growth" model (**Fig. S18**). While the cycled CF/Ag-CF@Zn electrode shows weaker Zn signal (9.23 wt%) and stronger carbon signal (55.67 wt%) from CF/Ag-CF interphase, indicating that Zn deposition mainly occurs at the bottom of dual-gradient interphase due to "bottom-top" deposition mode rather than "top-growth" model.

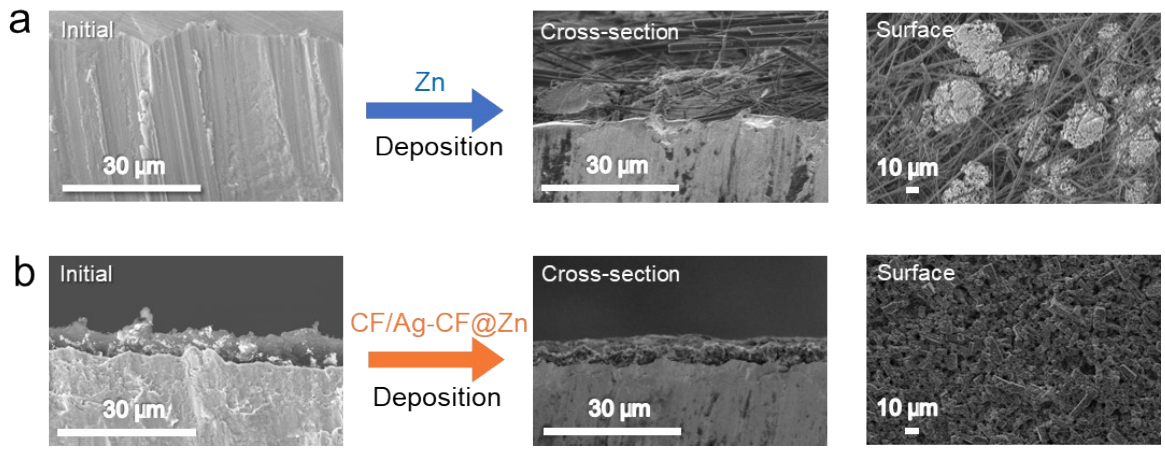

Fig. S19. SEM images of (a) Zn and (b) CF/Ag-CF@Zn after deposition with 1 mAh cm^{-2} at 1 mA cm^{-2}.

Notes to Fig. S19: The deposited Zn is densely confined at the bottom of the dual-gradient interphase without Zn-dendrites at the anode/separator interface. Meanwhile, there is no obvious plated Zn deposit on the surface of CF/Ag-CF@Zn. However, rampant zinc particles appear at the Zn/separator interface and even extend into the glass fiber separator to form protruding dendrites during the bare Zn deposition process, which are prone to causing short circuits. These results verify that CF/Ag-CF@Zn suppresses adverse "top-growth" dendrites on Zn anodes.

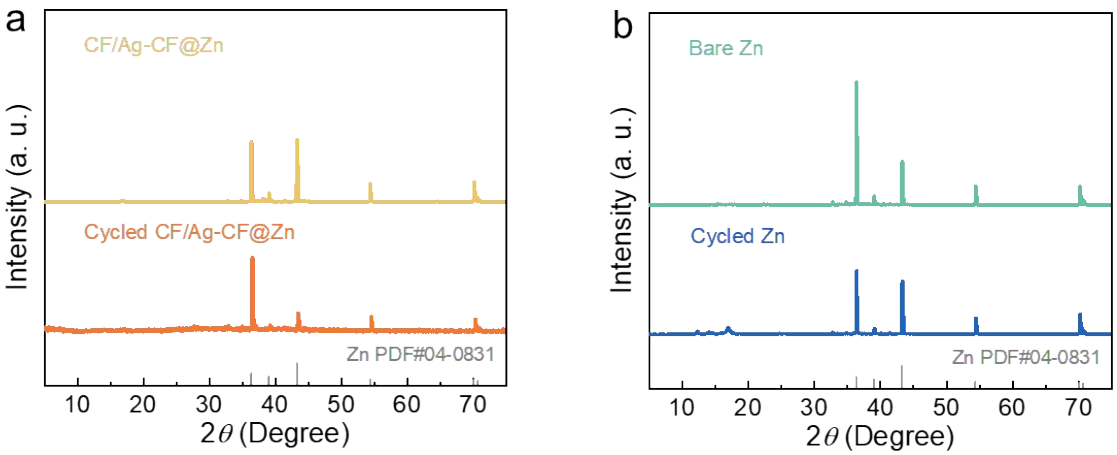

Fig. S20. XRD patterns for (a) CF/Ag-CF@Zn and (b) bare Zn before and after 30 cycles.

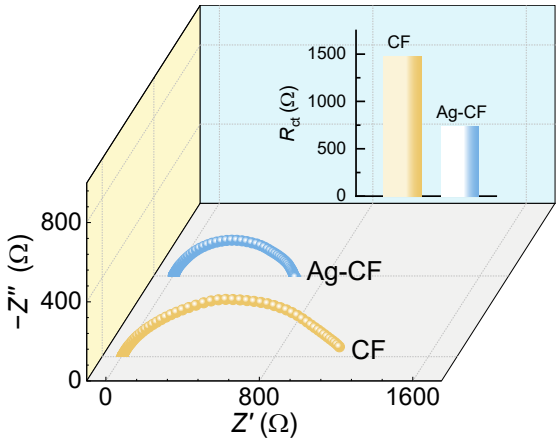

Fig. S21. EIS of symmetric cells using the CF@Zn and Ag-CF@Zn.

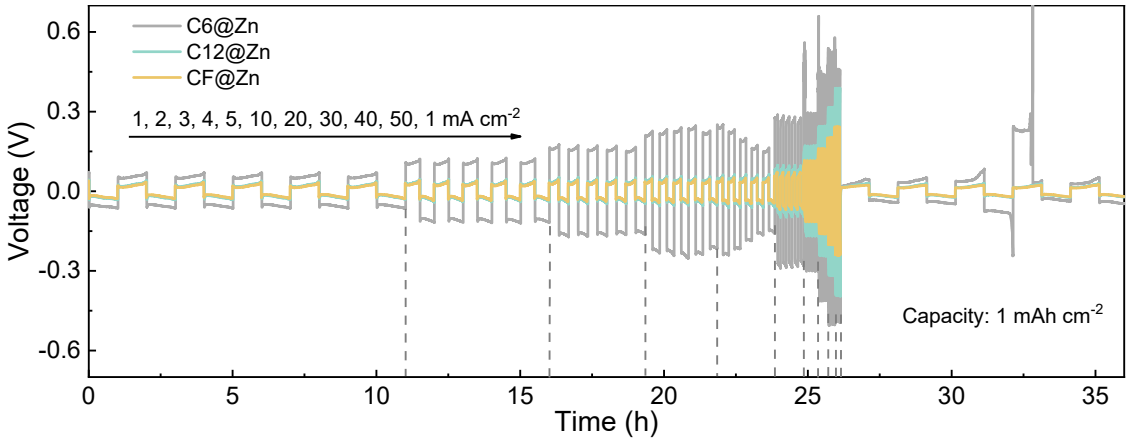

Fig. S22. Rate performance of symmetric zinc cells with different carbon interphases.

Notes to Fig. S22: The symmetric zinc cell with CF@Zn possesses a substantially steadier performance and lower overpotential than that employing the C6 and C12. This can be explained by the fact that CF has a larger surface and regular porous fiber architecture, which can enhance initial nucleation sites and facilitate electrolyte transport.[17]

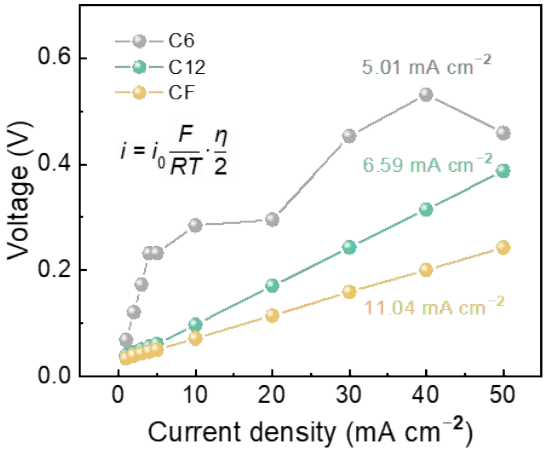

Fig. S23. Exchange current density from curves at various rates in symmetric zinc cells with different carbon interphases.

Notes to Fig. S23: The exchange current density is commonly employed to evaluate the kinetics of Zn deposition (Equation S1, Supporting Information).[5] The symmetric zinc cell with CF@Zn exhibits a higher exchange current density of 11.04 mA cm^{-2} compared to C6 (5.01 mA cm^{-2}) and C12 (6.59 mA cm^{-2}), suggesting that CF underpins efficient Zn deposition kinetics.

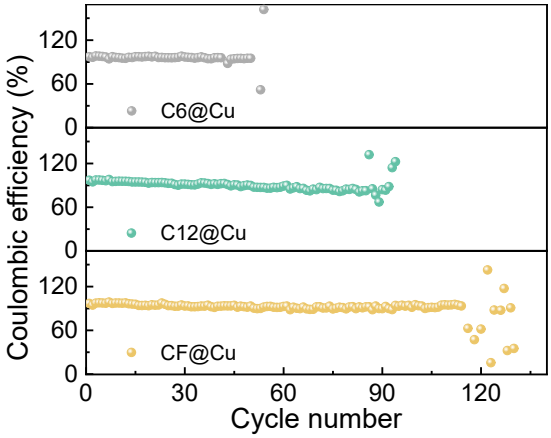

Fig. S24. Coulombic efficiency (CE) of asymmetric cells with different carbon electrodes at 1 mA cm^{-2} for 1 mAh cm^{-2}.

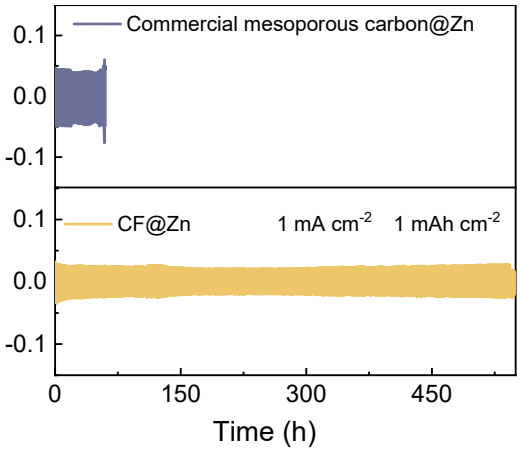

Fig. S25. GCD profiles of symmetric zinc cells with commercial mesoporous carbon and CF interphases at 1 mA cm^{-2} for 1 mAh cm^{-2}.

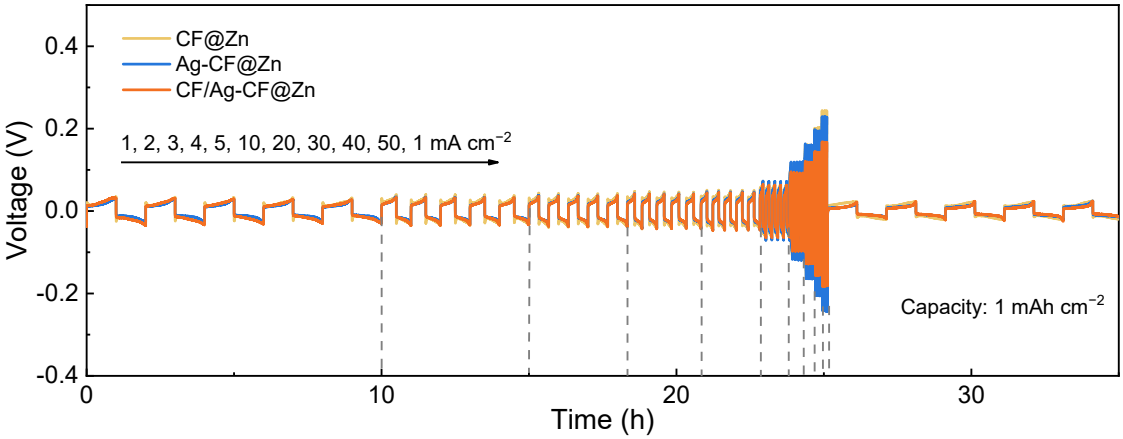

Fig. S26. Rate performance of symmetric zinc cells with different gradient interphases.

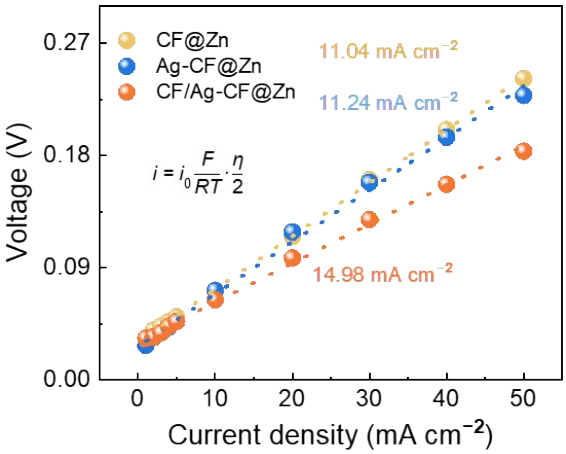

Fig. S27. Exchange current density from curves at various rates in symmetric zinc cells with different gradient interphases.

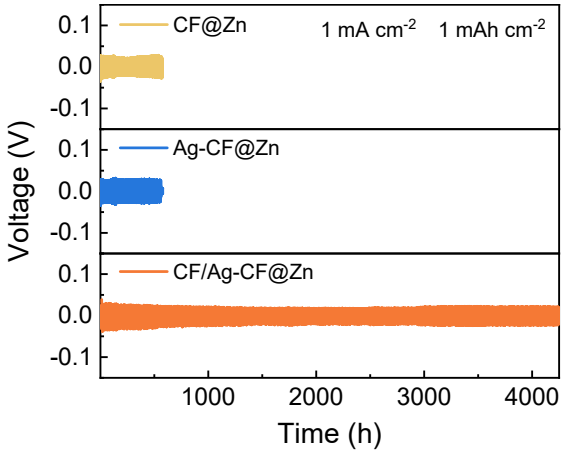

Fig. S28. GCD profiles of symmetric zinc cells with different gradient interphases at 1 mA cm^{-2} for 1 mAh cm^{-2}.

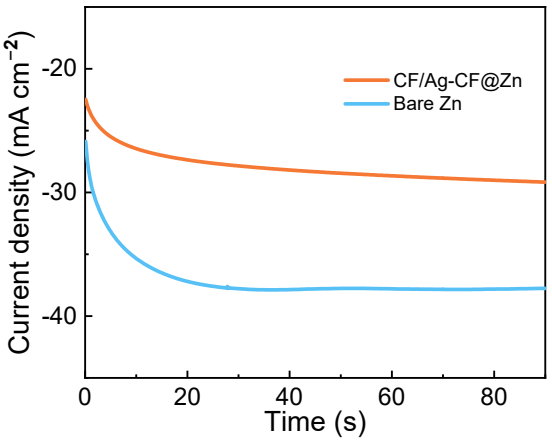

Fig. S29. CA profiles at an overpotential of −200 mV versus the open circuit potential using a three-electrode system.

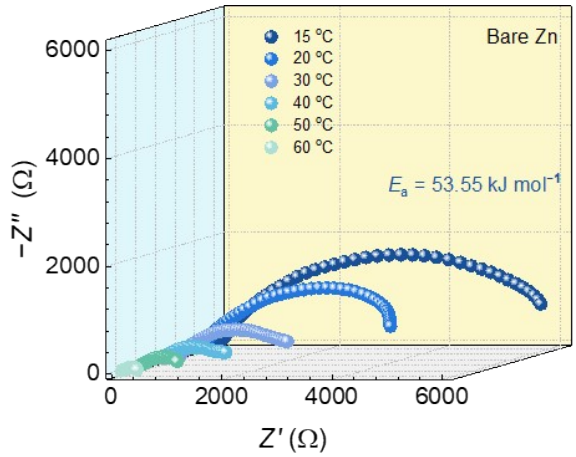

Fig. S30. EIS of bare Zn symmetric cell at different temperatures and E_a value.

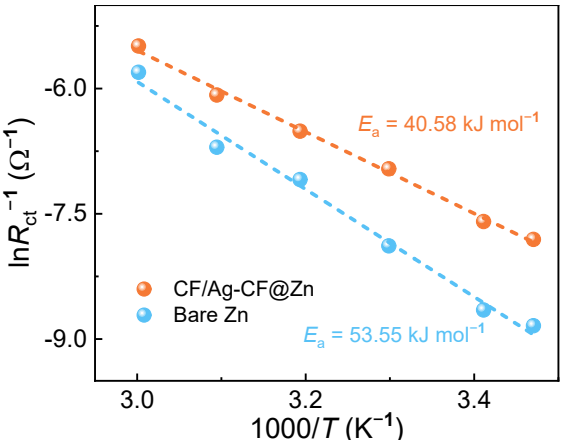

Fig. S31. E_a values of CF/Ag-CF@Zn and bare Zn.

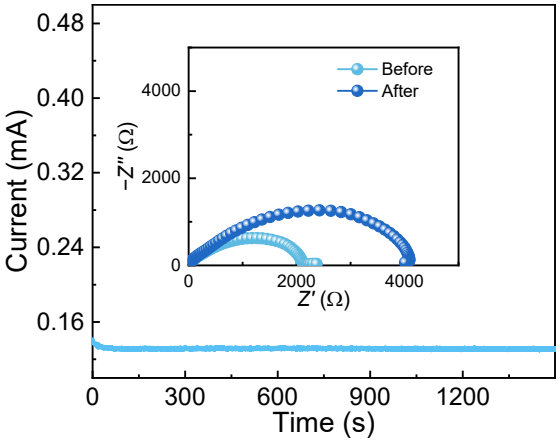

Fig. S32. Current-time curve of bare Zn symmetric cell at 20 mV (inset is EIS before and after CA test).

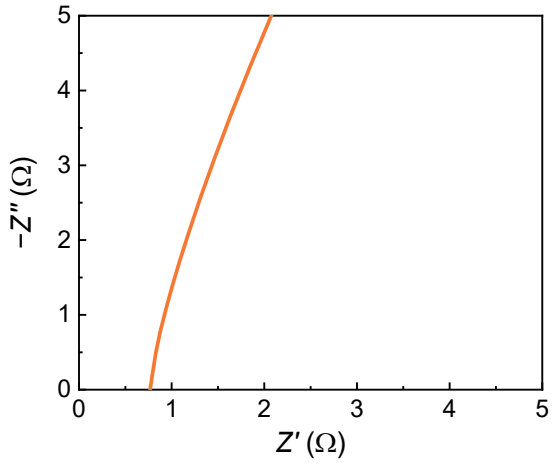

Fig. S33. EIS result of the symmetric cell in CF/Ag-CF@Cu||CF/Ag-CF@Cu

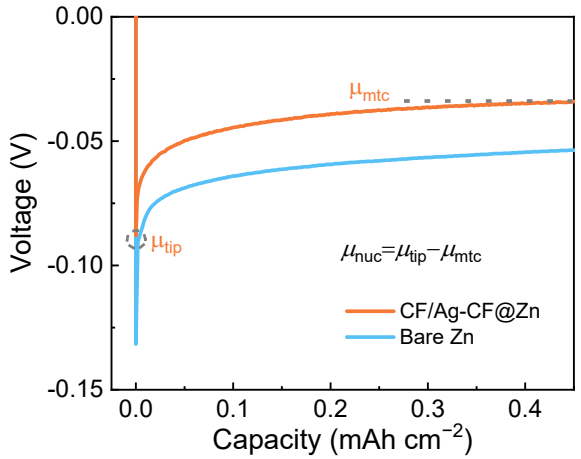

Fig. S34. Voltage profiles of Zn deposition on CF/Ag-CF@Zn and bare Zn symmetric cells at 1 mA cm^{-2}.

Notes to Fig. S34: The nucleation overpotential (μ_{nuc}) is defined as the difference between the tip potential (μ_{tip}) and the mass-transfer-controlled potential (μ_{mtc}).[18]

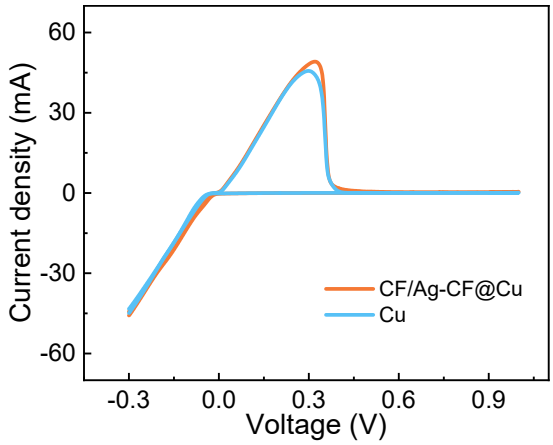

Fig. S35. CV curves of the asymmetric cells with CF/Ag-CF@Cu and Cu electrodes.

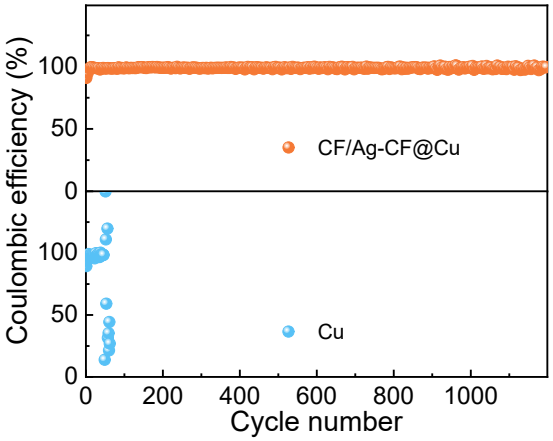

Fig. S36. CE of the asymmetric cells with CF/Ag-CF@Cu and Cu electrodes at 1 mA cm^{-2} for 1 mAh cm^{-2}.

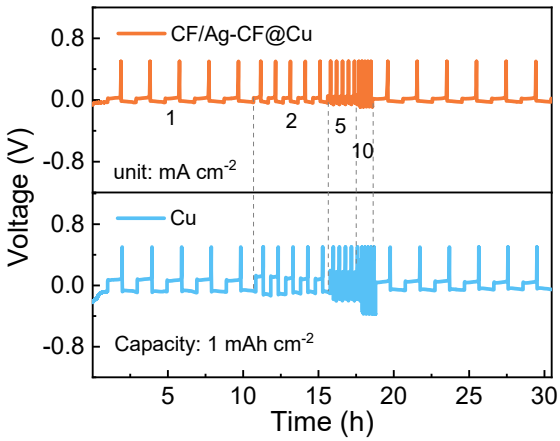

Fig. S37. Rate performance of asymmetric cells with CF/Ag-CF@Cu and Cu electrodes.

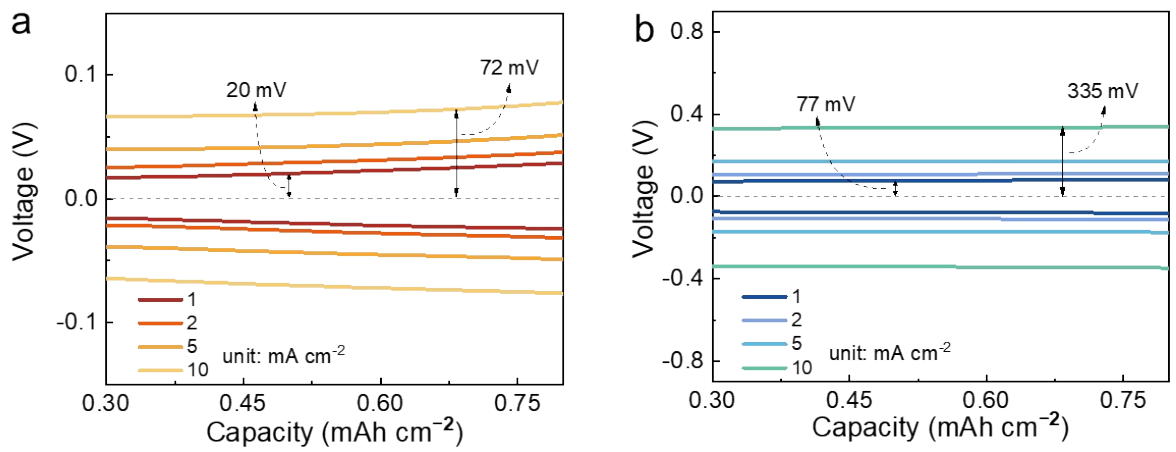

Fig. S38. Voltage profile of (a) CF/Ag-CF@Cu and (b) Cu electrodes in the asymmetric cell at various rates with a capacity of 1 mAh cm^{-2}.

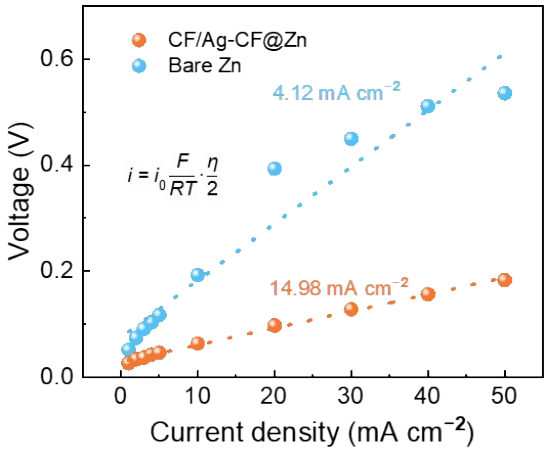

Fig. S39. Exchange current density from curves at various rates in CF/Ag-CF@Zn and bare Zn symmetric cells.

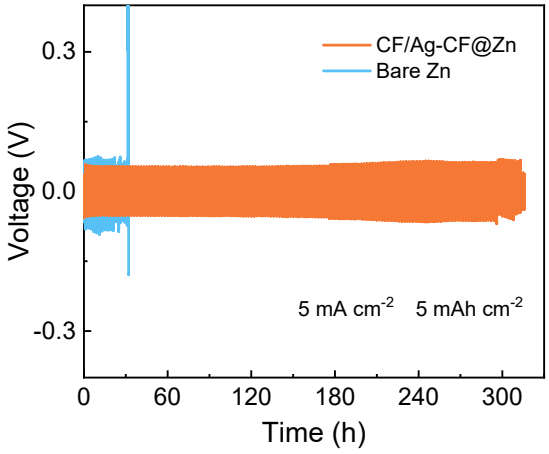

Fig. S40. GCD curves of CF/Ag-CF@Zn and bare Zn symmetric cells at 5 mA cm^{-2} for 5 mAh cm^{-2}.

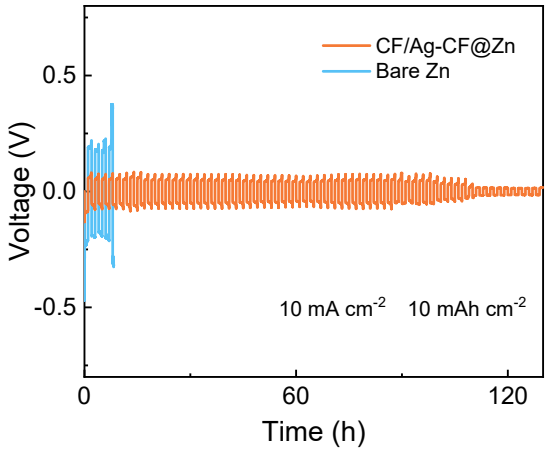

Fig. S41. GCD of CF/Ag-CF@Zn and bare Zn symmetric cells at 10 mA cm^{-2} for 10 mAh cm^{-2}.

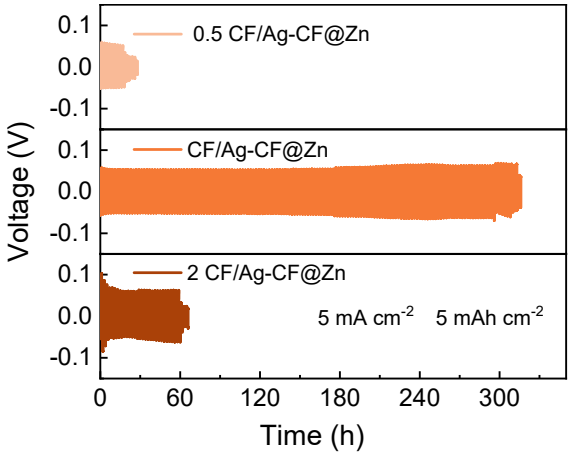

Fig. S42. GCD curves of CF/Ag-CF@Zn with different thickness at 5 mA cm^{-2} for 5 mAh cm^{-2}.

Notes to Fig. S42: To understand the influence of artificial interphase thickness by adjusting the height of the scraper, galvanostatic cycling experiments of CF/Ag-CF interphase with different thicknesses were carried out. Based on the CF/Ag-CF@Zn step-by-step slurry coating method, Zn foil was coated with Ag-CF and CF slurries sequentially using a doctor blade with a height of 20 μm and 40 μm. The same method was also used to prepare interphase with twice the thickness reduction and twice the thickness expansion, named 0.5 CF/Ag-CF and 2 CF/Ag-CF, respectively.

Table S3. Comparison of electrochemical performance metrics of symmetric cells.

Order	Zn host	Current density & Capacity ($mA\ cm^{-2}$ & $mAh\ cm^{-2}$)	Cycle time (h)	Accumulation capacity ($Ah\ cm^{-2}$)	Refs.
1	CF/Ag-CF@Zn	5.00 & 1.00	6700	16.75	This work
2	ACG-SEI	20 5	2000	20	19
3	FCOF@Zn	40 & 1	750	15.00	20
4	ZS-PEG400-KBr	18.00 & 18.00	1600	14.40	21
5	PSPMA@Zn	10.00 & 5.00	2500	12.50	22
6	Zn@ZBO	60.00 & 2.00	400	12.00	23
7	SIR@Zn	10.00 & 10.00	2000	10.00	24
8	TCNQ	20.00 & 5.00	1000	10.00	25
9	PPZn	10.00 & 1.00	1800	9.00	26
10	Sn@Zn	20.00 & 5.00	900	9.00	27
11	ZSB@Zn	5.00 & 2.50	3100	7.75	28
12	ZP-coated zinc	20.00 & 1.00	750	7.50	29
13	ZHP@Zn	10.00 & 1.00	1200	6.00	30
14	EBP-NG/Zn	4.00 & 1.00	2970	5.94	31
15	ZP@Zn	5.00 & 1.25	2000	5.00	32
16	COP-CMC/QG	5.00 & 3.00	2000	5.00	33
17	MMT-Zn	10.00 & 45.00	1000	5.00	34
18	HB-ZnHCF@Zn	10.00 & 5.00	1000	5.00	35
19	Cu-MXene-Zn	10.00 & 1.00	1000	5.00	36
20	BR-Zn	5.00 & 1.00	1970	4.93	37

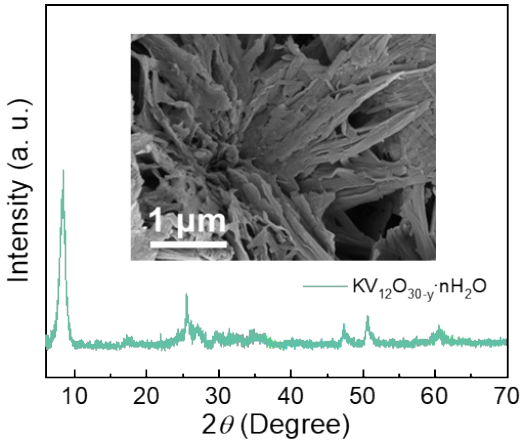

Fig. S43. XRD pattern and SEM image of the synthesized $KV_{12}O_{30-y}·nH_2O$ (KVOH).

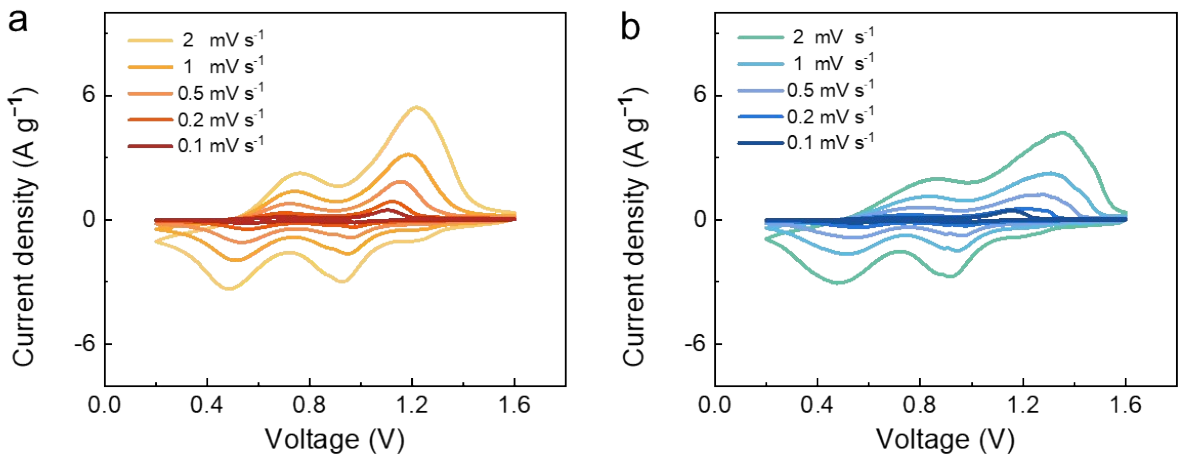

Fig. S44. CV curves of (a) CF/Ag-CF@Zn||KVOH and (b) Zn||KVOH full cells at different scan rates.

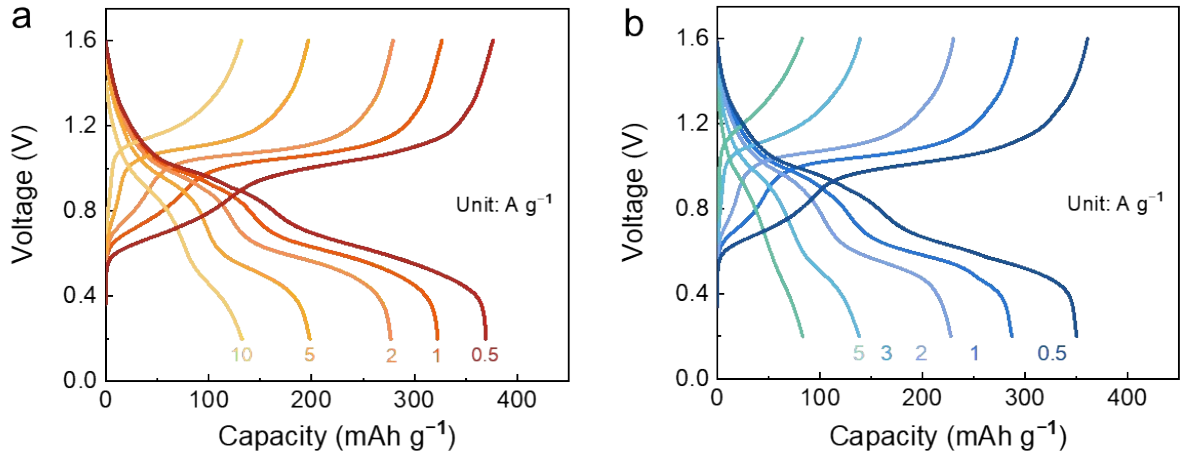

Fig. S45. GCD curves of (a) CF/Ag-CF@Zn||KVOH and (b) Zn||KVOH full cells at different current densities.

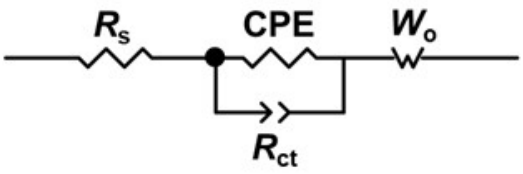

Fig. S46. The equivalent circuit used for fitting the experimental EIS data of full cells.

Table S4. EIS parameters of charge transfer resistance (R_{ct}) and similar equivalent series resistance (R_s) for CF/Ag-CF@Zn||KVOH and Zn||KVOH full cells before and after 40 cycles.

Sample	Before cycling		After cycling	
	R_s	R_{ct}	R_s	R_{ct}
CF/Ag-CF@Zn||KVOH	6.16	3.67	6.21	298.83
Zn||KVOH	9.18	203.74	10.55	480.37

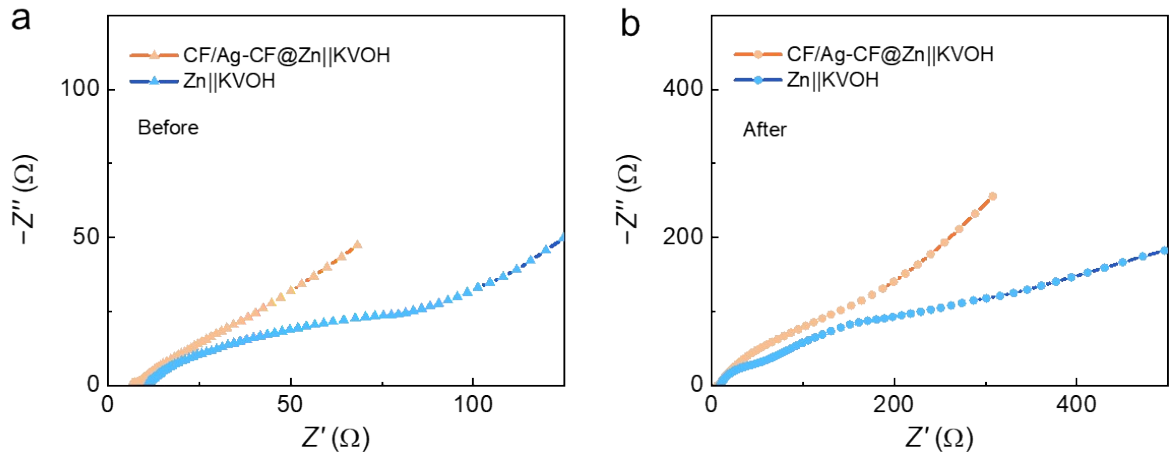

Fig. S47. EIS for (a) CF/Ag-CF@Zn||KVOH and (b) Zn||KVOH full cells before and after 40 cycles.

References

1. M. Zhou, S. Guo, J. Li, X. Luo, Z. Liu, T. Zhang, X. Cao, M. Long, B. Lu, A. Pan, G. Fang, J.

Zhou and S. Liang, *Adv. Mater.*, 2021, **33**, 2100187.

2. X. Yang, C. Li, Z. Sun, S. Yang, Z. Shi, R. Huang, B. Liu, S. Li, Y. Wu, M. Wang, Y. Su, S. Dou and J. Sun, *Adv. Mater.*, 2021, **33**, 2105951.
3. J. He, Y. Tang, G. Liu, H. Li, M. Ye, Y. Zhang, Q. Yang, X. Liu and C. Li, *Adv. Energy Mater.*, 2022, **12**, 2202661.
4. L. Wang, B. Zhang, W. Zhou, Z. Zhao, X. Liu, R. Zhao, Z. Sun, H. Li, X. Wang, T. Zhang, H. Jin, W. Li, A. Elzatahry, Y. Hassan, H. J. Fan, D. Zhao and D. Chao, *J. Am. Chem. Soc.*, 2024, **146**, 6199−6208.
5. J. B. Park, C. Choi, J. H. Park, S. Yu and D. W. Kim, *Adv. Energy Mater.*, 2022, **12**, 2202937.
6. Y. Zeng, X. Zhang, R. Qin, X. Liu, P. Fang, D. Zheng, Y. Tong and X. Lu, *Adv. Mater.*, 2019, **31**, e1903675.
7. X. Xie, S. Liang, J. Gao, S. Guo, J. Guo, C. Wang, G. Xu, X. Wu, G. Chen and J. Zhou, *Energy Environ. Sci.*, 2020, **13**, 503−510.
8. T. H. Wan, M. Saccoccio, C. Chen and F. Ciucci, *Electrochim. Acta*, 2015, **184**, 483−499.
9. F. Ciucci and C. Chen, *Electrochim. Acta*, 2015, **167**, 439−454.
10. M. B. Effat and F. Ciucci, *Electrochim. Acta*, 2017, **247**, 1117−1129.
11. J. Liu, T. Wan and F. Ciucci, *Electrochim. Acta*, 2020, **357**, 136864.
12. O. Turkarslan, A. Erden, E. Sahin and L. Toppare, *J. Macromol. Sci. Part A-Pure Appl. Chem.*, 2007, **43**, 115−128.
13. S. Mallakpour and A. Zadehnazari, *Synth. Met.*, 2013, **169**, 1−11.
14. M. Kalinowska, G. Świderski and W. Lewandowski, *Polyhedron*, 2009, **28**, 2206−2218.
15. Z. Song, L. Miao, L. Ruhlmann, Y. Lv, D. Zhu, L. Li, L. Gan and M. Liu, *Adv. Mater.*, 2021, **33**, 2104148.
16. X. Qiu, X. Wang, Y. He, J. Liang, K. Liang, B. L. Tardy, J. J. Richardson, M. Hu, H. Wu, Y. Zhang, O. J. Rojas, I. Manners and J. Guo, *Sci. Adv.*, 2021, **7**, eabh3482.
17. G. Liang, J. Zhu, B. Yan, Q. Li, A. Chen, Z. Chen, X. Wang, B. Xiong, J. Fan, J. Xu and C. Zhi, *Energy Environ. Sci.*, 2022, **15**, 1086−1096.
18. M. S. Kim, J.-H. Ryu, Deepika, Y. R. Lim, I. W. Nah, K.-R. Lee, L. A. Archer and W. Il Cho, *Nat. Energy*, 2018, **3**, 889−898.
19. X. He, Y. Cui, Y. Qian, Y. Wu, H. Ling, H. Zhang, X. Y. Kong, Y. Zhao, M. Xue, L. Jiang

and L. Wen, *J. Am. Chem. Soc.*, 2022, **144**, 11168–11177.

20. Z. Zhao, R. Wang, C. Peng, W. Chen, T. Wu, B. Hu, W. Weng, Y. Yao, J. Zeng, Z. Chen, P. Liu, Y. Liu, G. Li, J. Guo, H. Lu and Z. Guo, *Nat. Commun.*, 2021, **12**, 6606.
21. S. Jin, Y. Deng, P. Chen, S. Hong, R. Garcia-Mendez, A. Sharma, N. W. Utomo, Y. Shao, R. Yang and L. A. Archer, *Angew. Chem. Int. Ed.*, 2023, **62**, e202300823.
22. H. Liu, Q. Ye, D. Lei, Z. Hou, W. Hua, Y. Huyan, N. Li, C. Wei, F. Kang and J. Wang, *Energy Environ. Sci.*, 2023, **16**, 1610−1619.
23. D. Wang, H. Liu, D. Lv, C. Wang, J. Yang and Y. Qian, *Adv. Mater.*, 2023, **35**, 2207908.
24. H. Du, R. Zhao, Y. Yang, Z. Liu, L. Qie and Y. Huang, *Angew. Chem. Int. Ed.*, 2022, **61**, e202114789.
25. P. Xiong, C. Lin, Y. Wei, J.-H. Kim, G. Jang, K. Dai, L. Zeng, S. Huang, S. J. Kwon, S.-Y. Lee and H. S. Park, *ACS Energy Lett.*, 2023, **8**, 2718–2727.
26. S. H. Baek, J. S. Byun, H. J. Kim, S. J. Lee, J. M. Park, P. Xiong, Y. G. Chung and H. S. Park, *Chem. Eng. J.*, 2023, **468**, 143644.
27. Q. Jiao, X. Zhai, Z. Sun, W. Wang, S. Liu, H. Ding, W. Chu, M. Zhou and C. Wu, *Adv. Mater.*, 2023, **35**, 2300850.
28. Z. Wang, H. Chen, H. Wang, W. Huang, H. Li and F. Pan, *ACS Energy Lett.*, 2022, **7**, 4168−4176.
29. H. J. Kim, S. Kim, K. Heo, J. H. Lim, H. Yashiro and S. T. Myung, *Adv. Energy Mater.*, 2022, **13**, 2203189.
30. X. Qian, L. Li, Y. Wang, Z. Tian, H. Zhong, W. Chen, T. Chen and J. Fu, *Energy Storage Mater.*, 2023, **58**, 204–214.
31. C. Fan, W. Meng, D. Li and L. Jiang, *Energy Storage Mater.*, 2023, **56**, 468–477.
32. Z. Xing, Y. Sun, X. Xie, Y. Tang, G. Xu, B. Lu, J. Han, S. Liang, G. Chen and J. Zhou, *Angew. Chem. Int. Ed.*, 2022, **62**, e202215324.
33. J. Ding, Y. Liu, S. Huang, X. Wang, J. Yang, L. Wang, M. Xue, X. Zhang and J. Chen, *ACS Appl. Mater. Interfaces*, 2021, **13**, 29746–29754.
34. H. Yan, S. Li, Y. Nan, S. Yang and B. Li, *Adv. Energy Mater.*, 2021, **11**, 2100186.
35. M. Liu, W. Yuan, G. Ma, K. Qiu, X. Nie, Y. Liu, S. Shen and N. Zhang, *Angew. Chem. Int. Ed.*, 2023, **62**, e202304444.

36.Y. Li, Q. Zhu, M. Xu, B. Zang, Y. Wang and B. Xu, *Adv. Funct. Mater.*, 2023, **33**, 2213416.

37.Z. Yang, C. Hu, Q. Zhang, T. Wu, C. Xie, H. Wang, Y. Tang, X. Ji and H. Wang, *Angew. Chem. Int. Ed.*, 2023, **62**, e202308017.